Posted on 16 Mar 2023 — The copyright holder is the author/funder. All rights reserved. No reuse without permission. — https://doi.org/10.22541/essoar.167898495.56032750/v1 — This a preprint and has not been peer reviewed. Data may be preliminary.

# Assessing impacts of environmental perturbations on urban biogenic carbon exchange in the Chicago region

Peiyuan Li[1], Ashish Sharma[1], Zhihua Wang[2], and Donald J. Wuebbles[3]

[1]University of Illinois System
[2]Arizona State University
[3]University of Illinois at Urbana Champaign

March 16, 2023

**Abstract**

Carbon dioxide (CO2) quantification is critical for assessing city-level carbon emissions and sustainable urban development. While urban vegetation has the potential to provide environmental benefits, such as heat and carbon mitigation, the CO2 exchange from biogenic sectors and its impact from the environmental perturbations are often overlooked. It is also challenging to simulate the plant functions in the complex urban terrain. This study presents a processed-based modeling approach to assess the biogenic carbon fluxes from the vegetated areas over the Chicago Metropolitan Area (CMA) using the Weather Research and Forecast - Urban Biogenic Carbon exchange (WRF-UBC) model. We investigate the change of CO2 sink power in CMA under heatwaves and irrigation. The results indicate that the vegetation plays a significant role in the city's carbon portfolio and the landscaping management has the potential to reduce carbon emissions significantly. Furthermore, based on the competing mechanisms in the biogenic carbon balance identified in this study, we develop a novel Environmental Benefit Score metrics framework to identify the vulnerability and mitigation measures associated with nature-based solutions (NbS) within CMA. By using the generalized portable framework and our science-policy confluence analysis presented in this study, global cities can maximize the effectiveness of NbS and accelerate carbon neutrality.

**Hosted file**

`958543_0_art_file_10794245_rrh0yb.docx` available at https://authorea.com/users/595676/articles/629532-assessing-impacts-of-environmental-perturbations-on-urban-biogenic-carbon-exchange-in-the-chicago-region

**Hosted file**

`958543_0_supp_10794246_rrh0yb.docx` available at https://authorea.com/users/595676/articles/629532-assessing-impacts-of-environmental-perturbations-on-urban-biogenic-carbon-exchange-in-the-chicago-region

# Assessing impacts of environmental perturbations on urban biogenic carbon exchange in the Chicago region

**Peiyuan Li[1], Ashish Sharma[1,2,4], Zhi-Hua Wang[3] and Donald Wuebbles[1,4]**

[1] *Discovery Partners Institute, University of Illinois System, Chicago, IL 60606 USA*

[2] *Environmental Science Division, Argonne National Laboratory, Lemont, IL 60439 USA*

[3] *School of Sustainable Engineering and the Built Environment, Arizona State University, Tempe, AZ 85205 USA*

[4] *Department of Atmospheric Sciences, University of Illinois at Urbana-Champaign, Champaign, IL 61820 USA*

**Abstract**

Carbon dioxide ($CO_2$) quantification is critical for assessing city-level carbon emissions and sustainable urban development. While urban vegetation has the potential to provide environmental benefits, such as heat and carbon mitigation, the $CO_2$ exchange from biogenic sectors and its impact from the environmental perturbations are often overlooked. It is also challenging to simulate the plant functions in the complex urban terrain. This study presents a processed-based modeling approach to assess the biogenic carbon fluxes from the vegetated areas over the Chicago Metropolitan Area (CMA) using the Weather Research and Forecast - Urban Biogenic Carbon exchange (WRF-UBC) model. We investigate the change of $CO_2$ sink power in CMA under heatwaves and irrigation. The results indicate that the vegetation plays a significant role in the city's carbon portfolio and the landscaping management has the potential to reduce carbon emissions significantly. Furthermore, based on the competing mechanisms in the biogenic carbon balance identified in this study, we develop a novel Environmental Benefit Score metrics framework to identify the vulnerability and mitigation measures associated with nature-based solutions (NbS) within CMA. By using the generalized portable framework and our science-policy confluence analysis presented in this study, global cities can maximize the effectiveness of NbS and accelerate carbon neutrality.

**Keywords:** urban biogenic $CO_2$ exchange, land use, urban heat, irrigation, mitigation and adaptation

## Plain Language Summary

Urban plants modify the built environment and can absorb carbon dioxide. But their behaviors have not been fully studied in the urban setting, nor have the impacts of the urban environment on the growth of plants. In this study, we use a numerical model to co-simulate the urban environment and the behaviors of urban green land to investigate their interactions in the Chicago Metropolitan Area. The results show that heatwave will decrease the overall carbon absorption; while proper irrigation can help capture more carbon dioxide from the air. Compared to the traffic emissions in the Chicago region, the variations of carbon absorption are over 35%, which is considered significant. Moreover, we investigate the underlying mechanisms that lead to the outcomes and point out the corresponding measures to reduce the negative impact. This study will potentially guide the cities to achieve better environmental benefits from urban green spaces and contribute to carbon reduction.

## 1. Introduction

Globally, cities are now home to more than half of the population (UN-Habitat, 2020). Cities have experienced rapid expansion and densification, making them hotspots of anthropogenic heat and emissions, contributing to localized urban heat island (UHI) effects as well as global-scale climate change (Churkina, 2016; Oke et al., 2017). Dense urban population pockets with low resources and limited adaptive capacity, in turn, become particularly vulnerable to climate change impacts (Melillo et al., 2014). Many cities have implemented climate action plans (CAPs) to build preparedness and resilience and guide future planning and decision-making (Castán Broto and Westman, 2020). Nature-based solutions (NbS), usually referred to as urban greening, are widely recommended in CAPs as their dual function in UHI mitigation and carbon reduction (Kabisch et al., 2017), and the environmental-friendly and cost-effective features (Frantzeskaki et al., 2019). The City of Chicago, for example, envisioned the human well-being and biodiversity benefits of NbS since its first CAP in 2008. In the 2022 update, Chicago centers on the role of NbS and continues to expand the installment of green infrastructures as one of many other specific actions (Chicago, 2022). The regional CAP for the Chicago Metropolitan Area (CMA), which covers the City of Chicago and its surrounding developed land, also encourages NbS wherever feasible to mitigate the consequences of climate change over the Great Lakes Region (Makra and Gardiner, 2021; Wuebbles et al., 2019, Wuebbles et al., 2021).

Despite the high expectation of NbS, their function was rarely assessed quantitatively, especially in the urban environment and under meteorological and anthropogenic perturbations. In past decades, most efforts to quantify $CO_2$ emissions from cities have been focused on anthropogenic sources (e.g., buildings and transportation), as these sources typically dominate urban emissions (Seto et al., 2012). The $CO_2$ exchange from the biogenic sectors varies significantly in different climate regions (Yi et al., 2010), weather events (Lei and Han, 2020; Xu et al., 2020), land use types (McHale et al., 2017), and landscaping practices (Crum et al., 2016). Its proportionality in a city's carbon portfolio can be surprisingly high under specific conditions. Prior studies reported that the behavior of urban plants tends to have greater uncertainties under the warming from UHI and $CO_2$ fertilization effect (i.e., vegetation growth benefited from high $CO_2$ concentration) from anthropogenic emissions (Zhao et al., 2016; Zhou et al., 2016; Wang et al., 2019b) (Fig. 1a), altering the carbon balance (Fig. 1b). These impacts from urbanization on

plant function can be intensified by sudden increases of temperature (e.g., during heatwaves or high heat days, Fig. 1d&e), which is yet underexplored and worth thorough investigations.

Additionally, human management of urban green spaces affects $CO_2$ exchange as well. For example, irrigation, which helps urban plants growth and serves as a mitigation measure for extreme urban heat (Livesley et al., 2021), can lead to the environmental co-benefits in cooling and carbon reduction (Li and Wang, 2021) (Fig. 1f). Conversely, over-irrigation may cause unintended $CO_2$ release from soil respiration (Decina et al., 2016; Hundertmark et al., 2021; Kindler et al., 2022), offsetting $CO_2$ absorption from photosynthesis (Fig. 1g). The lack of consensus indicates the large spatial variation of biogenic $CO_2$ efflux that different mechanisms could govern. It also implies the potential to enhance carbon reduction from urban greenery by avoiding unintended $CO_2$ release and/or increasing $CO_2$ sequestration. Therefore, for cities that consider NbS for carbon reduction, it is critical to understand the interplays in the heat-water-carbon nexus in urban environments and the underlying mechanisms corresponding to the geographical and meteorological characteristics of the highly heterogeneous urban land use.

Current approaches for estimating urban biogenic $CO_2$ exchange primarily rely on the data collected from urban eddy covariance (EC) systems (Crawford et al., 2011; Velasco and Roth, 2010; Velasco et al., 2013; Ng et al., 2015) and remote sensing (RS) imagery (McPherson et al., 2013; Hardiman et al., 2017; Miller et al., 2018). The EC system measures total $CO_2$ flux as well as other meteorological variables at a high temporal resolution and can relate $CO_2$ emissions to local land use features and weather events (Järvi et al., 2019; Liu et al., 2012). However, its applications are limited to neighborhood scale due to its small footprint (~1 $km^2$). Multisite studies are usually required to account for urban heterogeneity (Bergeron and Strachan, 2011; Park et al., 2022). Additional efforts for flux decomposition are also required to distinguish biogenic signals from their anthropogenic counterparts (Menzer and McFadden, 2017; Salgueiro et al., 2020; Stagakis et al., 2019). RS-based algorithms can examine spatial patterns over a large area and quantify biogenic $CO_2$ exchange by employing statistical and machine learning methods over the remotely sensed variables such as land surface temperature, land use types, vegetation indices, etc. (Zhao and Running, 2010; Rossini et al., 2012). Nonetheless, the relatively long overpass period of the satellites makes the RS approach more capable of interpreting the seasonal trend than the hourly dynamics.

In addition to the measurement-based approaches, process-based models such as vegetation photosynthesis and respiration models (VPRM), light use efficiency models (LUE), and solar-induced fluorescence models (SIF) are widely used to quantify biogenic $CO_2$ exchanges over natural biomes (Gourdji et al., 2022; Madani et al., 2017; Li and Xiao, 2019). These models are able to run numerical experiments with future climate projections. Recent attempts were seen to implement process-based simulations in an urban environment, mainly from two distinctive approaches: the "top-down" and "bottom-up" approach. The "top-down" approach treats cities as a combination of impervious and natural surfaces and quantifies $CO_2$ exchange based on plant types, coverage, and biomass density (Wu et al., 2021). In fact, the behaviors of urban plants are under the influence of UHI, elevated $CO_2$ levels, and landscaping maintenance (Smith et al., 2019; Fu et al., 2021). These factors need to be accounted when estimating biogenic $CO_2$ exchange in cities. The "bottom-up" approach resolves the complex hydroclimate dynamics in urban street canyons using single-layer urban canopy schemes and drives the photosynthesis and respiration models for ecosystem exchange (Goret et al., 2019; Li and Wang, 2020). Further integrating these "bottom-up" models with regional climate models, such as Weather Research and Forecast, can allow us to simulate the interplays between plant behaviors, the urban environment, and climate change at the city and/or regional scale.

To this end, this paper presents a model that quantifies urban biogenic $CO_2$ exchange with the resolved hydroclimate dynamics in urban street canyons. We further assess the impacts of environmental and anthropogenic perturbations, viz., heatwave and irrigation, on the urban biogenic $CO_2$ exchange and reveal the underlying controls from these environmental perturbations. Specifically, we estimate net ecosystem exchange (NEE), gross primary productivity (GPP), and ecosystem respiration ($R_{eco}$) over the Chicago Metropolitan Area (CMA) using the state-of-art Weather Research Forecast – Urban Biogenic Carbon model (WRF-UBC) under designed numerical experiments. Our analysis identifies the prevailing urban management practices in CMA and its sub-zones to enhance carbon reduction from urban greenery. The results will help the city officials and urban planners understand the variations of NbS regarding environmental perturbations, which will lead to better decision-making towards the "*zero-carbon*" goal.

## 2. Materials and Methods

### 2.1 Study area

We select the Chicago Metropolitan Area (CMA) to quantify the biogenic $CO_2$ exchanges. CMA is the third most populated region in the United States. It has a highly developed urban core by the side of Lake Michigan with a radial urban-rural gradient extending away from the lakeshore. According to recent estimates from the US Census Bureau in 2010 and Chicago Metropolitan Agency for Planning (CMAP) in 2018, 55% of the land in CMA is classified as a developed urban area with a diverse land use portfolio (Fig. 2a). Many studies have investigated the urban environment in terms of urban morphology (Patel et al., 2023), extreme heat (Sharma et al., 2016; Sharma et al., 2017), precipitation (Vavrus and Van Dorn, 2010), anthropogenic emissions (Conry et al., 2015) of this region, making CMA an ideal testbed for future urban climate studies. Meanwhile, the region is actively integrating adaptive NbS, primarily by implementing green urban design and increasing green spaces to mitigate hydrometeorological extremes and reduce $CO_2$ emissions (Makra and Gardiner, 2021). This is important as there has been an increase in the frequency of regional heat waves as a result of climate change in the Great Lakes Region (Wuebbles et al., 2019; Wuebbles et al., 2021).

### 2.2 WRF-UBC model

The Weather Research and Forecast - Urban Biogenic Carbon model couples the urbanized Weather Research and Forecast (uWRF) modeling framework (Skamarock et al., 2019; Chen et al., 2011) with process-based Arizona State Single Layer Urban Model (ASLUM, Li and Wang, 2020, Wang et al., 2021) to calculate the photosynthesis and respiration rates of vegetation in urban street-canyon environments. Both uWRF and ASLUM have been implemented in prior studies as a tool to examine urban heat and the corresponding mitigation strategies (Li and Wang, 2021; Li et al., 2022; Sharma et al., 2016; Georgescu et al., 2014; Wang et al., 2018). In this study, we adopt the surface and near-surface meteorological conditions estimated from uWRF (version 4.1, Skamarock et al., 2019) over CMA to drive ASLUM for the subsequent modeling of $CO_2$ fluxes. Specifically, we set up three two-way nested domains using WRF with the outermost boundary covering the Midwest US and the innermost domain covering the CMA and its surrounding rural and agricultural areas (Fig. 2b). The spatial resolutions of three domains are 9 km, 3 km, and 1 km, respectively. The lateral boundary conditions of the

uWRF simulation were provided by North American Regional Reanalysis (NARR) 32km by 32km from the National Center for Environmental Prediction (NCEP) at a 3-hour interval (https://rda.ucar.edu/datasets/ds608.0/). Physical schemes of microphysics, convection, radiation, and boundary layer were configured using a well-tested combination for the Chicago region as described in Sharma et al. (2017). The 30-m resolution National Land Cover Database (NLCD) 2016 is used to better reflect the land surface heterogeneity matching the simulation period. For the land surface dynamics, we select the single-layer urban canopy scheme for impervious urban surfaces and Noah-land surface model (Noah-LSM) for natural land and the pervious portion of the urban grids. Meteorological variables, such as downwelling shortwave radiation (SWD), windspeed ($U$), air humidity ($q$), air pressure ($P_a$), 2-meter air temperature ($T_2$), surface temperature ($T_s$), topsoil temperature ($T_{soil}$), are calculated every 180 seconds and aggregated to hourly output. The simulation period is from May 1 2016 00:00 UTC to August 31 2016 23:59 UTC (123 days), with the first 3 days as the spin-up period.

The urban gross primary productivity (GPP) and ecosystem respiration ($R_{eco}$) are subsequently estimated via the photosynthesis and respiration models in ASLUM. GPP is formulated as

$$\mathrm{GPP} = f_V \int_0^{LAI} F_{GPP}\left(PAR, T_{sk}, [\mathrm{CO_2}], U, \theta\right) dL, \qquad \text{Eq. (1)}$$

where function $F_{GPP}$ is a series of the $A_g$-$r_s$-type plant photosynthesis functions adopted in ASLUM; $f_v$ is vegetation fraction (-); LAI is the leaf area index ($m^2m^{-2}$); $PAR$ is photosynthetic activated radiation ($Wm^{-2}$); $T_{sk}$ is the leaf skin temperature ($^oC$); [$CO_2$] is near surface $CO_2$ concentration level (ppm); $U$ is the near-surface wind speed; $\theta$ is the normalized soil moisture in urban green spaces (-). The special integral aggregate leaf-level carbon assimilation rate to canopy-level primary productivity with the consideration of the light extinction inside of the canopy. The urban ecosystem respiration ($R_{eco}$) is calculated as

$$\mathrm{R_{eco}} = f_S F_{\mathrm{R}}\left(T_{\mathrm{soil}}, \theta, LAI\right), \qquad \text{Eq. (2)}$$

where $F_R$ is the temperature-dependent respiration function adopted in ASLUM; $f_s$ is soil fraction; and $T_{soil}$ is the temperature of the surface layer of soil ($^oC$). The detailed formulation of $F_{GPP}$ and $F_R$ is described in Ronda et al. (2001) and Li and Wang (2020). The hydroclimate variables, such as $T_{soil}$, $T_{sk}$, $U$, $\theta$, and $PAR$ in Eq.(1) and Eq.(2) are directly derived from uWRF simulation at the urban surface level, while the leaf area index, vegetation fractions, and background $CO_2$ level are

adopted from external spatial gridded data (see Section 2.3). The urban net ecosystem exchange (NEE) is calculated as

$$NEE = R_{eco} - GPP \cdot \quad \text{Eq. (3)}$$

NEE is directional. A positive value means a net release of $CO_2$ from urban green spaces, while a negative value means net $CO_2$ sequestration.

## 2.3 External datasets

To better resolve the heterogeneity of the complex urban terrains, we utilize the vegetation properties from Copernicus Global Land Service (CGLS), which provides LAI and vegetation fractions at a 300 m spatial resolution and a 10-day temporal interval (Fig. S1). CGLS has a better representation of the biomass spatiotemporal distributions, especially over urban areas. The use of CGLS will allow us to achieve finer spatial resolution when quantifying carbon exchanges, and avoid uncertainties induced by the imprecise vegetation data from the WRF modeling system (Vahmani and Ban-Weiss, 2016). The land surface $CO_2$ level is a critical parameter for the photosynthesis process as it determines the concentration gradient of $CO_2$ at the leaf-air interface (Tomimatsu and Tang, 2016). We adopt Carbon Tracker spatial gridded data (CT2019, Jacobson et al., 2020) to provide the ambient $CO_2$ concentration over the study area. The original dataset from CT2019 is linearly interpolated to match the spatiotemporal resolution of the innermost uWRF domain.

Apart from those essential data to drive WRF-UBC, observations from ground stations are used to calibrate and validate the simulation experiments. The base rate of respiration, usually represented by $R_{25}$ (respiration rate at 25 $^{o}$C), varies across climate zones. It is necessary to calibrate the parameters to local measurement to improve the credibility of the modeling results, especially for simulating at such a high spatiotemporal resolution (Li and Wang, 2020). We decompose the total carbon flux ($F_c$) measured by eddy covariance (EC) towers in CMA to calibrate the parameters in photosynthesis and respiration models. The EC towers (AmeriFlux ID: US-IB1 and US-IB2) are located over a cropland and grassland in Fermi National Accelerator Laboratory in the suburban region west of Chicago, respectively (Fig. 2c). The towers measured $F_c$ at 4.05 and 3.76 meters above the ground. Due to the relatively low measurement heights, the measured $F_c$ can be treated as a close proxy to NEE without the disturbance from anthropogenic $CO_2$ signals. Ecosystem respiration is derived from the nighttime $F_c$ when photosynthesis

completely stops in the absence of sunlight, which is commonly referred as the nighttime partitioning method (Reichstein et al., 2005). We first calibrate the parameters in Eq.(2) to fit the nighttime $F_c$ measured during 20:00 to 04:00 local time as the observation of nighttime $R_{eco}$. The calibrated Eq.(2) will be used to calculate $R_{eco}$ time-series (Fig. S2). Then the measured GPP can be obtained by subtracting the calculated $R_{eco}$ from the measured $F_c$. We again calibrate the parameters in Eq.(1) to match the daily mean value of GPP decomposed from the total $F_c$. The calibrated model performed reasonably well in replicating the temporal variations of $CO_2$ fluxes at the tower locations. It is worth mentioning that spatial coverage of high-quality carbon flux measurement in an urban environment is rather limited. There are also subsidiary uncertainties associated with source partitioning at each location. Thus, it is extremely challenging to validate the model performance spatially. As a result of this known caveat, our study will focus on comparing two different experimental scenarios (see Section 2.4). In this case, the calibration and validation against EC datasets will be sufficient to satisfy the objectives of our study.

The daily summaries of air temperature measured by ground weather stations in the Global Historical Climatology Network daily (GHCNd) from the National Centers for Environmental Information (NCEI) are used to validate the simulated 2-meter air temperature as a representative of the fundamental meteorological conditions. In addition, we also validate our results against the hourly air temperature measurements from Local Climatological Data (LCD) network. Figure 2c shows the locations of the ground weather stations. The model performance is evaluated using the root mean squared error (RMSE), calculated as

$$\mathrm{RMSE} = \sqrt{\frac{\sum (X_{\mathrm{sim}} - X_{\mathrm{obs}})^2}{n}}, \qquad \text{Eq. (4)}$$

where $X_{sim}$ is the model simulation; $X_{obs}$ is the observation from ground weather stations at daily or hourly intervals; $n$ is the number of observations. The model performs reasonably well with RMSEs of 2.17 $^{o}$C and 2.49 $^{o}$C over the daily and hourly observations (Fig. 2d). This accuracy is comparable to the model bias reported in the previous studies over the Contiguous United States (Wang et al., 2019a) and Chicago region (Sharma et al., 2017) using uWRF. The result on the magnitude and the spatial pattern of heat distribution provided us the confidence to use our model experiment design for subsequent modeling of photosynthesis and respiration processes.

## 2.4 Design of numerical experiments

In the first set of experiments, we test the impact of high heat on the biogenic $CO_2$ exchange in CMA. The 123-day simulation is divided into heatwave (HW) days and non-heatwave (non-HW) days according to the daily maximum and minimum air temperatures ($T_{max}$ and $T_{min}$). Specifically, we compare the modeled air temperature to the long-term daily climate normals, viz., average daily maximum and minimum temperatures ($T_{n,\,max}$ and $T_{n,\,min}$), derived from the ground measurements during 1991-2020 at 44 reference locations near CMA (Fig. S3). A heatwave day is identified when (1) both $T_{max}$ and $T_{min}$ exceed $T_{n,\,max}$ and $T_{n,\,min}$ respectively; (2) last longer than 2 days; and (3) over 90% reference locations meet (1) and (2). These criteria identify 31 heatwave days during the summer of 2016 (Fig. 3). By contrasting the biogenic $CO_2$ exchange rate during the HW and non-HW days, we can quantify the role of temperature on plant behaviors. The HW scenarios can also serve as a proxy for the future warming projection in CMA.

The second set of experiments investigates the impact of irrigation. While keeping the model configurations unaltered from the previous case (REF case hereafter), we re-run the model with urban irrigation turned on in uWRF (IRR case henceforth). The prescribed irrigation scheme waters the vegetated portion in urban cells to soil field capacity every night. This treatment is the default irrigation configuration in WRF v4.1 and can be easily replicated in modeling or in practice for the other regions. Urban irrigation is expected to directly increase the soil water content and indirectly decrease the temperatures by reducing sensible heat and redistributing available surface energy fluxes (Broadbent et al., 2018; Wang et al., 2019a). As photosynthesis and respiration processes are sensitive to soil water availability and temperatures, irrigation will affect biogenic $CO_2$ exchange via multiple mechanisms, potentially leading to an optimum irrigation scheme for environmental co-benefits in cooling and carbon reduction (Li and Wang, 2021).

These two sets of experiments will demonstrate the change of biogenic $CO_2$ flux under environmental and anthropogenic perturbations. As a result, we report the changes in value and percentage over the CMA and for different land use types.

## 3. Result and Discussion

### 3.1 Biogenic $CO_2$ exchange in CMA

The NEE over the urbanized area is calculated using the calibrated WRF-UBC (Fig. 4). During the simulation period, the daily mean NEE over CMA is −2.4 g $m^{-2}d^{-1}$ with a wide range of spatial variation primarily correlated with land use type (Fig. 2a) and biomass density (Fig. S1). Regions with high vegetation fraction ($f_v$) and leaf area index (LAI) tend to have lower NEE (higher carbon sequestration rate), represented by the riparian parks along the Des Plaines River and the sparsely distributed urban forests in CMA. The NEE in these urban parks is −6.7 g $m^{-2}d^{-1}$, followed by those undeveloped (−2.7 g $m^{-2}d^{-1}$) and residential areas (−2.5 g $m^{-2}d^{-1}$). These exchange rates convert to a total $CO_2$ sink of $-1.5\times10^4$ metric tons of $CO_2$ per day ($tCO_2$/day) in CMA from urban vegetation, dominated by residential areas (41.8%, $-6.3\times10^3$ $tCO_2$/day) and urban parks (40.9%, $-6.1\times10^3$ $tCO_2$/day). The other land use types account for 45.6% of the land but contributed only 17.3% to carbon sequestration. Vegetated land in commercial and industrial areas releases $CO_2$ to the atmosphere (Fig. S4b), although the amount is very subtle ($0.3\times10^3$ $tCO_2$/day).

3.2 Impacts of heatwaves

During the 31 heatwave (HW) days, the daily mean and maximum temperature are 25.0 $^oC$ and 30.1 $^oC$, respectively, which are 5.0 $^oC$ and 5.3 $^oC$ hotter compared to the non-heatwave (non-HW) days with significant differences ($p<0.001$) in diurnal cycles. It is worth mentioning that despite the high temperatures during HW episodes, no extreme drought condition is observed due to the occasional precipitations during the summer of 2016 (Fig. 3). The difference in soil water content (SWC) between HW and non-HW days are negligible (Fig. S5a). During HW days, we observe an overall increase of NEE from $-1.7\times10^4$ $tCO_2$/day to $-0.8\times10^4$ $tCO_2$/day with a relatively homogenous distribution over CMA (Fig. 6a). Note that the increase in NEE is not caused by the slowdown of biochemical reactions due to high temperatures. On the contrary, the high temperature stimulates the biochemical processes and drastically promotes the GPP and $R_{eco}$ by 16.8% and 38.6%, respectively (Fig. 5a). It is evident that the respiration rate increases faster than the photosynthesis rate, resulting in a net increase in NEE. The distinctive rate change can be attributed to the different locations of photosynthesis and ecosystem respiration. More specifically, $R_{eco}$ consists primarily of plant above-ground respiration, root respiration, and soil respiration, with the first process happening in the air and the rest two occurring underground. As soil respiration occurs outside of the vegetation, its rate is not strictly coupled with

photosynthesis. As a result of the differences in the responses of photosynthesis and respiration to the same environmental perturbation, net biogenic carbon fluxes will vary. We discuss the underlying mechanisms in further detail in Section 3.4.

Figures 6b&c show the change of GPP, and $R_{eco}$ (dGPP, $dR_{eco}$), respectively. The spatial patterns generally follow the distribution of vegetation fraction and LAI, meaning areas with higher biomass will be more susceptible to a higher temperature. For example, urban parks, which have over 80% of vegetation coverage and 3.3 $m^2m^{-2}$ LAI, have the largest dNEE of 1.5 g $m^{-2}d^{-1}$ from −7.1 to −5.4 g $m^{-2}d^{-1}$ (Fig. 7a). No significant correlation is observed when examining the relations between the averaged dNEE of each land type to the other factors, such as mean air and soil temperatures or soil water content (Fig. S5 upper panel). In addition, there is no discernable difference in the rise of temperatures among different land use types. As a result, we conclude that biomass density plays a critical role in determining the impact of heatwave on $CO_2$ exchange.

### 3.3 Impacts of irrigation

In the irrigation experiment, the soil is irrigated to a preset threshold every night (see Section 2.3). The irrigation leads to an average increase of SWC by 7.0% over CMA (Fig. S5d). Meanwhile, the average temperatures of air ($T_2$) and soil ($T_{soil}$) are reduced by 0.3 $^oC$ and 2.8 $^oC$, respectively. The total NEE in the irrigation case is $-2.3\times10^4$ $tCO_2$/day (Fig. 6d). Compared to the reference case ($-1.5\times10^4$ $tCO_2$/day), irrigation can help to capture $0.8\times10^4$ $tCO_2$/day during the summer of 2016. The significant carbon reduction is led by the increase of GPP (7.9%) and the decrease of $R_{eco}$ (−4.8%) (Fig. 7b). In this case, the irrigation-induced environmental changes (i.e., cooling and moisturizing) form a pair of competing mechanisms affecting photosynthesis and respiration in separate and opposite ways. Specifically, cooling will slow down biochemical reactions, decrease GPP and $R_{eco}$, and moisturizing will stimulate vegetation growth and promote soil respiration. Intriguingly, the cooling effect from irrigation is more notable in soils than in the air. Therefore, irrigation suppresses soil respiration more than photosynthesis, leading to overall net carbon capture. We discuss these mechanisms further in Section 3.4.

Vegetation in residential yards exhibits the most significant change in NEE, contributing 44.1% in the total capture of $0.8\times10^4$ $tCO_2$/day. The next highest segment is the vegetation in urban parks (19.7%), followed by those along roads and streets (15.9%). Unlike the results from

the heatwave experiment, the spatial distribution of dNEE in the irrigation experiment does not follow the biomass distribution strictly (Fig. 6d, c.f. Fig. S1). The spatial patterns of dGPP and $dR_{eco}$ do not show meaningful associations either (Fig. 6e&f). Generally, GPP is governed by solar irradiance, ambient $CO_2$ level, air temperature, soil moisture, and plant biomass. In this experiment, we assume similar solar irradiance and $CO_2$ levels between irrigation and the reference cases. We use the same biomass density from CGLS in both simulations. Therefore, the change of GPP is mainly affected by the variations of air temperature and soil water content. The result shows that the averaged irrigation-induced air cooling is 0.3 $^{o}$C, with a maximum air cooling of ~0.5 $^{o}$C in the western part of CMA (Fig. S5e). The limited air cooling does not have a significant impact on GPP. Contrary to the minor air cooling, we observe a homogeneous increase in soil water (Fig. S5d). The magnitude of dGPP is enhanced by the biomass density, demonstrated in the densely vegetated residential areas to the immediate north and west of the urban core (Fig. 6e, c.f. Fig. S1). We also notice that a small area in the northwest region of CMA does not significantly change of GPP despite its moderate vegetation coverage. The likely reason for this is the modest increase in soil moisture in this area compared to the others.

The change of ecosystem respiration ($dR_{eco}$) shows distinctive spatial distribution from dGPP (Fig. 6f). Qualitatively, $R_{eco}$ will increase under higher soil temperature and higher moisture. However, irrigation cools down the environment and adds soil water simultaneously, affecting $R_{eco}$ in opposite ways: the lower temperature decreases $R_{eco}$; while the higher soil moisture increases $R_{eco}$. This forms a group of competing mechanisms, which offsets each other when influencing the overall $dR_{eco}$. For example, the west CMA shows a manifest decrease in soil temperature and a moderate increase in soil water content (Fig. S5e&f). These lead to little change in $R_{eco}$ in this area (Fig. 6f). In the northwest area of CMA, where dGPP is small, exhibits a noticeable decline of $R_{eco}$. This occurs when the weak "moisturizing" effect encounters a relatively strong "cooling" effect on respiration. We will explain the rationale for this mechanism in Section 3.4.

Surprisingly, we do not observe an apparent increase in $R_{eco}$ over CMA, which contradicts some observation-based studies (Decina et al., 2016; Kindler et al., 2022). One hypothesis suggests that excessive amounts of soil water will continuously enhance $R_{eco}$, while the cooling effect will cease once the irrigation exceeds certain thresholds (Li and Wang, 2021). In our experiment, the irrigation stops when the soil water content reaches the prescribed

threshold, mimicking the operation of on-demand smart irrigation systems, thus may prevent further increase of $R_{eco}$ due to excessive soil water (Fig. 1g c.f. Fig. 1f). However, in practice, a typical timed or metered irrigation system supplies water regardless of weather conditions and cannot control soil moisture accurately. This may directly cause the increase in $CO_2$ release reported in observation-based studies. The City of Chicago initiated the MeterSave program (https://metersave.org/MeterSave) in 2018. It offers irrigation systems equipped with rain gauges and moisture sensors for its residents, which will regulate water use and avoid excessive water supply like the irrigation experiment conducted in this study. Nonetheless, adopting a smart irrigation system in every residential yard is impractical. Our numerical experiments illustrate the potential for carbon reduction from urban irrigation when an optimized scheme is implemented (Yang and Wang, 2015; Liu et al., 2021).

### 3.4 Competing mechanisms in $CO_2$ exchange

The most effective way to mitigate carbon emissions from urban vegetation is to increase GPP while decreasing $R_{eco}$ to achieve an overall increase in carbon sequestration. In this case study over CMA, we observe general improvements in carbon reduction by irrigation (i.e., dNEE < 0), resulting from two major groups of competing mechanisms. To better understand their individual contributions to outcomes, we introduce the Environmental Benefit Score (EBS) as a rating metric to simplify and quantify the impacts of high heat and irrigation on carbon and hydroclimate dynamics (Fig. 8). Positive scores (+1 and +2) are given if the changes under perturbations (i.e., temperature and water supply changes) contribute positively and reduce $CO_2$ emission. Likewise, negative impacts will have negative scores (−1 and −2). We further denote the results using $\boldsymbol{EBS}(x)$, where $x$ can be the carbon, temperature, or water components (dGPP, $dR_{eco}$, drought, or water supply) under environmental and anthropogenic perturbations.

In the heatwave group, for example, the outcome depends on the individual impacts of humidity and temperature on $R_{eco}$ and GPP. Therefore, we have

$$\boldsymbol{EBS}(\text{dNEE}) = \boldsymbol{EBS}(\text{Humidity}) + \boldsymbol{EBS}(dR_{eco}) + \boldsymbol{EBS}(\text{dGPP}). \quad \text{Eq. (5)}$$

The simulation shows that dNEE > 0 over the entire CMA region during a heatwave shows negative environmental impacts (Fig. 6a). Meanwhile, dGPP > 0 and $dR_{eco} > 0$ with the change of $R_{eco}$ a high magnitude. Therefore, we give $\boldsymbol{EBS}(\text{dGPP}) = +1$, while $\boldsymbol{EBS}(dR_{eco}) = -2$. Since there is no drought during heatwaves in our experiment; we have $\boldsymbol{EBS}(\text{Humidity}) = 0$. These lead

415 to ***EBS***(dNEE) = −1 (Fig. 8a), which matches the simulation result. If a drought occurred while
416 other changes remained the same, the outcome would shift to "Worst" as ***EBS***(Humidity) = −1,
417 and ***EBS***(dNEE) = ***EBS***(Humidity) + ***EBS***($dR_{eco}$) + ***EBS***(dGPP) = −2 (Fig. 8b).
418 The mechanisms in the irrigation group are more complicated, as irrigation
419 simultaneously lowers temperature (cooling) and adds water supply (moisturizing). Both effects
420 will oppositely change GPP and $R_{eco}$, as mentioned in Section 3.3. In this case, the dNEE is
421 affected by their separate impacts on GPP and $R_{eco}$, leading to various outcomes as shown in
422 Figure 8 Group 2, and can be expressed as:
423 $$\boldsymbol{EBS}(dNEE) = \boldsymbol{EBS}(dNEE_M) + \boldsymbol{EBS}(dNEE_C)$$
424 $$= [\boldsymbol{EBS}(dR_{eco,\,M}) + \boldsymbol{EBS}(dGPP_M)] + [\boldsymbol{EBS}(dR_{eco,\,C}) + \boldsymbol{EBS}(dGPP_C)]. \quad \text{Eq. (6)}$$
425 where the subscript "M" and "C" represents the change induced by "moisturizing" and "cooling",
426 respectively. Eq. (6) shows the net impact of a certain mechanism. It can also be regrouped as
427 $$\boldsymbol{EBS}(dNEE) = [\boldsymbol{EBS}(dR_{eco,\,M}) + \boldsymbol{EBS}(dR_{eco,\,C})] + [\boldsymbol{EBS}(dGPP_M) + \boldsymbol{EBS}(dGPP_C)], \quad \text{Eq. (7)}$$
428 to reflect the competing mechanisms on one specific carbon flux.
429 In the irrigation group, the different sub-zones of CMA exhibit distinctive behaviors (Fig.
430 8). From the simulation result, we find the moderate benefit in Zone 3 is primarily contributed by
431 the increase of GPP (***EBS***(dGPP) = 1, Fig. 6e). The change of $R_{eco}$, however, is muted
432 (***EBS***($dR_{eco}$) = 0, Fig. 6f) because of the competing processes between moisturizing and cooling
433 effect on respiration (black lines lead to Fig. 8c). Moreover, if we compare the moisturizing and
434 cooling effect on dNEE, it shows cooling effect contributes more to reduce $CO_2$ emissions from
435 urban vegetation. Thus Zone 3 is a cooling dominant zone (see Text S1 for a detail explanation).
436 Similarly, the carbon reduction in Zone 5 is led by the increase in GPP. But unlike Zone
437 3, Zone 5 is a moisturizing dominant zone, meaning the cooling-induced dGPP and $dR_{eco}$ offset
438 each other (Fig. 8f, Text S2). Zones 2 and 4 benefit from the reduction of $R_{eco}$ led by cooling,
439 while the change of GPP is insignificant. They are also moisturizing dominant zones (Fig. 8d,
440 Text S3). Among the five zones, Zone 1 has the most notable decrease in NEE and thus has the
441 highest EBS (Fig. 8e).
442 To achieve the best outcome like Zone 1, one needs to precisely regulate the irrigation for
443 a delicate balance to simultaneously avoid increasing in $R_{eco}$ due to moisturizing and decreasing
444 of GPP due to cooling. For instance, $R_{eco}$ in Zone 3 increases dramatically due to moisturizing
445 (***EBS***($dR_{eco,M}$) = −2). This negative impact can be alleviated by irrigating less or enhancing soil

drainage to control the soil water content in Zone 3. Distinctively, carbon reduction in Zone 5 can be promoted under a cooler environment, which needs the help of additional heat mitigation actions such as shading trees and cool roofs. Our results show that the impacts of irrigation on the urban core are minor due to limited vegetation fractions. For the highly developed area in the urban core, increasing biomass will be the most effective action for carbon reduction. Note that these scores represented the relative magnitude among the sub-zones in CMA rather than their absolute magnitude. Though Zone 1 had the most favorable result in the current set of experiments, its carbon reduction can still be improved by further increasing vegetation fraction or optimizing the growth condition of urban plants. These conclusions can be generalized according to the pathways and outcome categories illustrated in the EBS chart (Fig. 8), especially for users without much knowledge of numerical modeling and plant physiological functions.

## 4. Conclusions

In summary, this study highlights the importance of $CO_2$ exchange from biogenic sectors in assessing carbon footprint at a city level. As an example, when comparing annual average emissions from on-road traffic of CMA in 2015 ($2.3\times10^4$ $tCO_2$/day, Gurney et al., 2020) and total yearly emission ($CO_2$ equivalent) in 2017 ($8.5\times10^4$ $tCO_2$/day, Chicago, 2019), urban vegetation in CMA ($-1.5\times10^4$ $tCO_2$/day) offsets more than half of the traffic emissions during the simulation period and over a quarter of the total emission. Meanwhile, the active biochemical processes during warm months can be affected significantly by environmental and anthropogenic perturbations. High temperature caused by heatwaves reduces the $CO_2$ sink power from vegetated land by $0.9\times10^4$ $tCO_2$/day, which is equivalent to 39% of traffic emissions. As the frequency, intensity, and duration of heatwaves are expected to increase due to climate change (Perkins-Kirkpatrick and Lewis, 2020), urban regions will be even more vulnerable in terms of the rising temperatures along with the urban heat island effects, and the unexpected loss of carbon capture. On the contrary, urban irrigation helps mitigate heat and is usually considered a practical NbS. In addition, it increases $0.8\times10^4$ $tCO_2$/day of carbon capture, offsetting ~35% of traffic emissions in equivalent. However, the irrigation efficacy varies spatially and is governed by different mechanisms. Some regions are sensitive to excessive irrigation and should precisely regulate the soil water to avoid further respiration rate increases. The other regions will be benefited from an overall cooler environment.

Spatially, we also find that the vegetation in residential areas, urban parks, and along the road and streets play a vital role in the city's carbon portfolio. These three land use categories account for ~81% of total carbon sequestration in CMA. Fortunately, these lands are usually equipped with irrigation systems and managed. Through detailed modeling and evaluation of the Environmental Benefit Score chart, we demonstrate that urban vegetation is more than just a "cool refugee" to the built environment. However, given the widespread application of irrigation, its influence on carbon exchange should be carefully considered to ensure overall positive environmental impacts. Using EBS, we illustrate the possible outcomes and the entangled dynamics in the heat-water-carbon nexus under anthropogenic forcings, with the goal of improving our understanding of urban vegetation carbon balance. The modeling framework described above can be applied to other cities and broader regions where the land use data are available.

It is noteworthy that the heatwaves do not coincide with severe drought conditions during our experiment. Although we observe a significant loss of carbon capture due to heatwaves, the situation can be even worse in the event of compounded extremes, which happened in the history of CMA. For example, two months before the heatwave on July 4-7$^{th}$ 2012, the precipitation in Illinois was 7.42 inches below average, making it the 3$^{rd}$ driest season in the state's history. Drought can increase evaporative demand and lead to fast depletion of soil moisture, thereby impeding biochemical activities (see Fig. 1d) or even leading to the death of vegetation. In this case, the potential GPP improved by warming will likely be offset by water constraints (Madani et al., 2020). Urban irrigation will prevent plants from severe drought and help them maintain normal biochemical processes when rainfall is insufficient. However, these processes are sensitive to soil water, and irrigation needs to be regulated to avoid unnecessary $CO_2$ emission or the loss of sink power.

Meanwhile, we reckon a few caveats in this study, such as the limited in-situ validation data and the hypothetical irrigation scheme. These limitations are primarily constrained by computational and observational resources. In conjunction with the highly heterogeneous urban surfaces, the lack of data makes it exceptionally difficult and computationally intensive to conduct the numerical experiments presented in this study. Despite these caveats, we hope the analysis could shed light on the decision-making towards carbon reduction from NbS and facilitate urban-centric climate projects such as the ongoing Community Research on Climate

and Urban Science (CROCUS) project sponsored by the US Department of Energy. The future implementation of WRF-UBC should incorporate a comprehensive database of the study area, such as the actual irrigation scheme, water use, proposed land use, zoning policies, etc., for better estimations of the current and future scenarios. It is also critical to consider other real-world constraints such as water resources, cost of maintenance and labor, etc. However, capturing these dynamics will need even more extensive numerical experiments from high-resolution modeling (Sharma et al., 2021) or even the help of advanced machine-learning techniques (Li et al., 2022). The future extension of this work will aim to provide a more holistic perspective on NbS via multi-objective optimization for carbon reduction.

**Acknowledgment**

This research is supported by the Walder Foundation and NSF award #139316. This work is also supported by the U.S. Department of Energy, Office of Science, Biological and Environmental Research, under contract DE-AC02-06CH11357. We would like to acknowledge high-performance computing support from Cheyenne (doi:10.5065/D6RX99HX) provided by NCAR's Computational and Information Systems Laboratory, sponsored by the National Science Foundation. CarbonTracker CT2019B results provided by NOAA ESRL, Boulder, Colorado, USA from the website at http://carbontracker.noaa.gov. We also acknowledge Metropolitan Mayors Caucus, NOAA, City of Chicago, and Chicago Metropolitan Agency for Planning for providing the data used in this study.

**Conflict of Interests**

The authors declare that they have no known competing financial interests or personal relationships that could have appeared to influence the work reported in this paper.

**Open Research Statement**

All the datasets used in this study are publicly available with open access under the CC-BY-4.0 license: CT2019B data at https://gml.noaa.gov/ccgg/carbontracker/. GHCNd dataset at https://www.ncei.noaa.gov/products/land-based-station/global-historical-climatology-network-daily. EC towers US-IB1 and US-IB2 via AmeriFlux site at https://ameriflux.lbl.gov/sites/siteinfo/US-IB1 and https://ameriflux.lbl.gov/sites/siteinfo/US-IB2. Land use of CMA at https://www.cmap.illinois.gov/data.

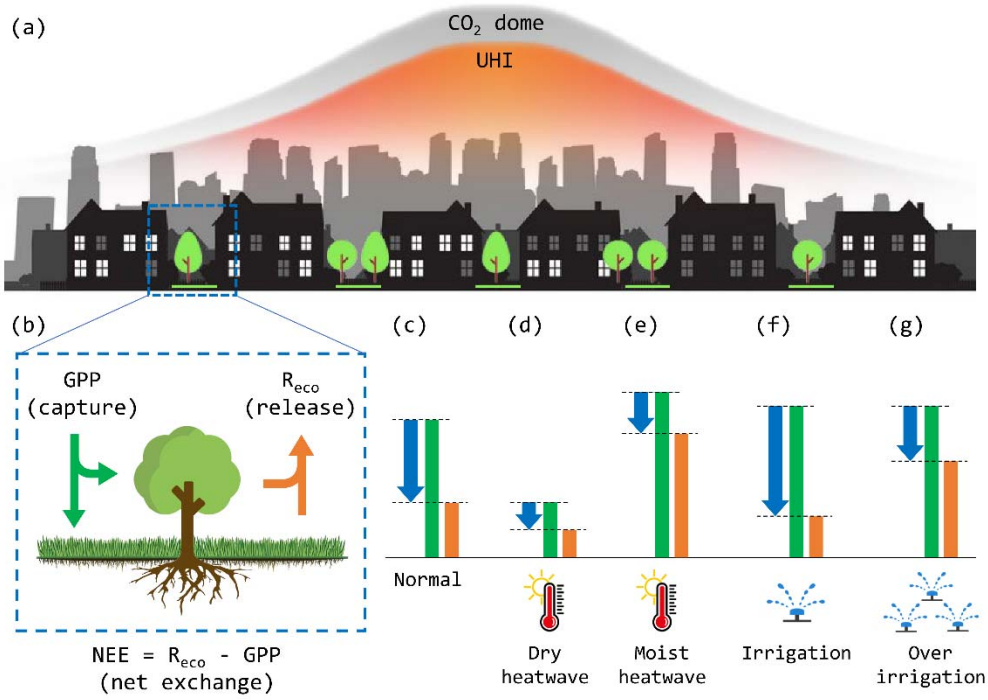



**Figure 1**. **Diagrams of biogenic carbon exchange in urban areas. (a)** Plants in cities live under high ambient $CO_2$ concentration and high temperature (UHI). (**b)** Biogenic carbon balance in urban vegetation (Eq. 3). **(c-g).** Qualitative illustrations of carbon balance under normal, dry heatwave, moist heatwave, irrigation, and over-irrigation conditions, respectively. The length of bars and arrows in subplot (**c-g**) show the magnitude of carbon fluxes. Blue, green, and orange colors represent NEE, GPP, and $R_{eco}$, respectively. Comparing to normal condition (c), dry heatwave (d) damages plant physiological functions and suppresses $CO_2$ exchange rate due to severe water stress. On contrary, moist heatwave (e) stimulates $CO_2$ exchanges with high temperature without water stress. Proper irrigation (f) adds water and reduce temperature, leading to environmental co-benefits in cooling and carbon reduction. Excessive irrigation (g) will likely cause significant increase of $R_{eco}$, leading to less carbon sequestration comparing to proper irrigation (f).

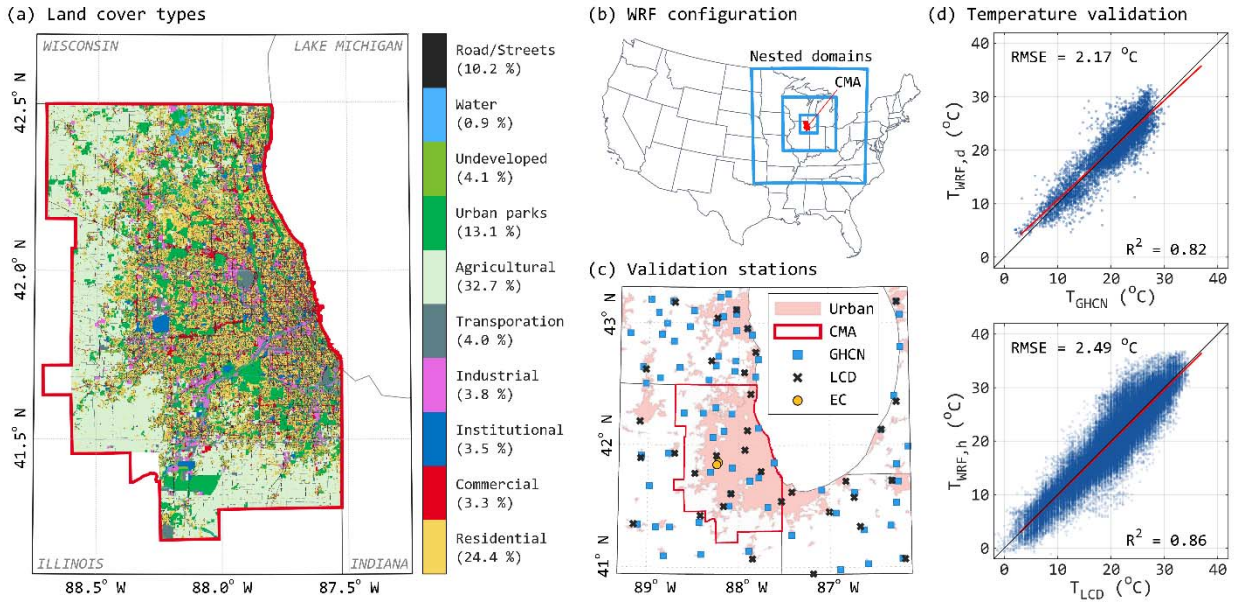
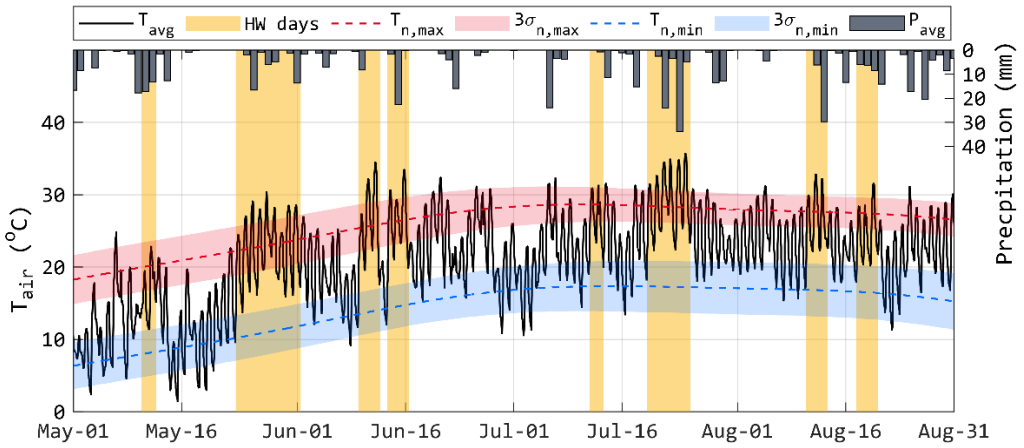



**Figure 2. (a)** Land cover types of CMA; **(b)** Domain configuration in WRF; **(c)** Locations of ground weather stations and EC towers used for model calibration and validation in this study; **(d)** The comparisons of daily (upper panel) and hourly (lower panel) air temperatures from WRF model and ground weather stations. GHCN - Global Historical Climatology Network; LCD - Local Climatological Data; EC - eddy covariance towers (US-IB1 & US-IB2).




565

566 **Figure 3. Identification of heatwave days.** The figure also shows the simulated hourly mean air
567 temperature (black line) and observed daily precipitation (overhead black bars) over CMA
568 during the study period. Dashed lines indicate the long-term climate normals in terms of daily
569 maximum (red, $T_{n,max}$) and minimum (blue, $T_{n,min}$) temperatures. The shaded areas along the
570 dashed lines show the variations (three standard deviations) among the reference stations. The
571 identified heatwave days are marked by the yellow shaded areas.
572

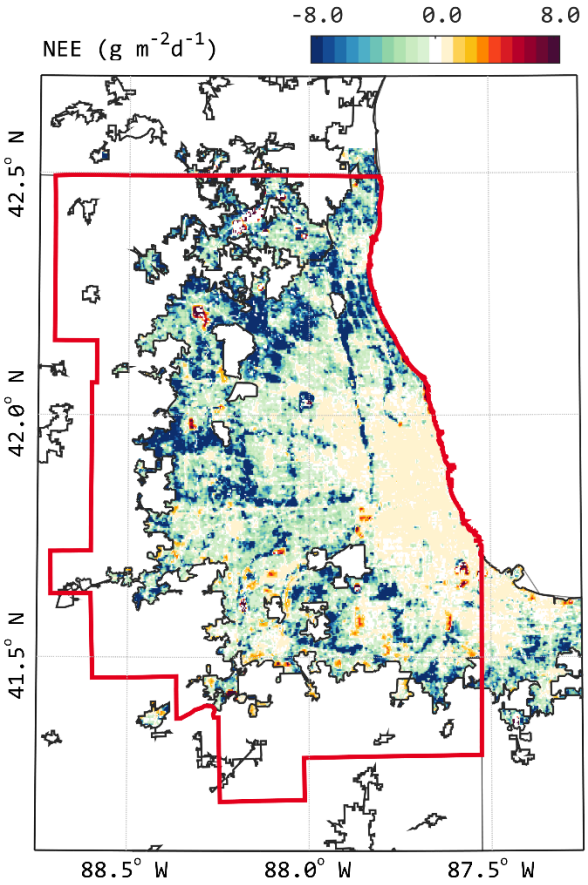
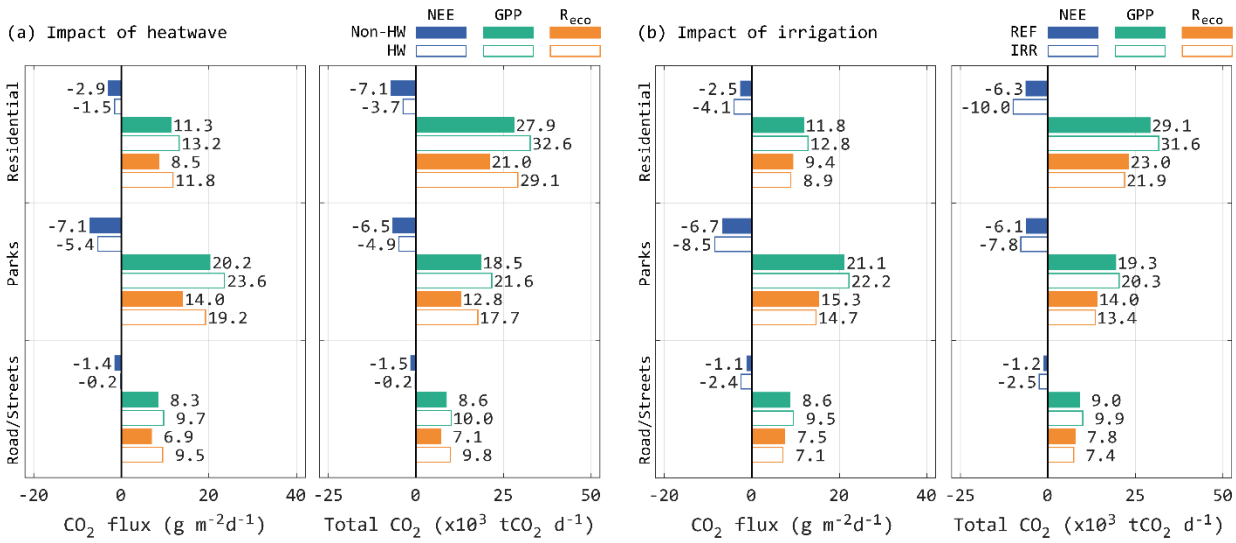



**Figure 4**. **Daily mean net ecosystem exchange (NEE) over urbanized areas in CMA.** Negative values (cool colors) represent net absorption of $CO_2$ from urban vegetation, vice versa. Red lines indicate the administrative boundary of the counties containing CMA. Black lines show the boundary of urban areas from 2010 US Census data, which excluding the agricultural and preserved natural land. The special urban boundary used in this study is the intersection of the two boundaries. All statistics in text and figures are calculated within this special urban boundary.




584

585 **Figure 5. Summary of biogenic $CO_2$ exchange by land use category. (a)** heatwave (HW) vs.
586 non-heatwave (non-HW); and **(b)** irrigation (IRR) vs. non-irrigation (REF). Blue, green, and
587 orange colors represent NEE, GPP, and $R_{eco}$, respectively. Only land use categories with
588 meaningful vegetation coverage are shown here: residential, maintained parks, and road/streets.
589 See Fig. S4 for the full chart of other categories (commercial, institutional, industrial,
590 transportation, undeveloped).

591

592

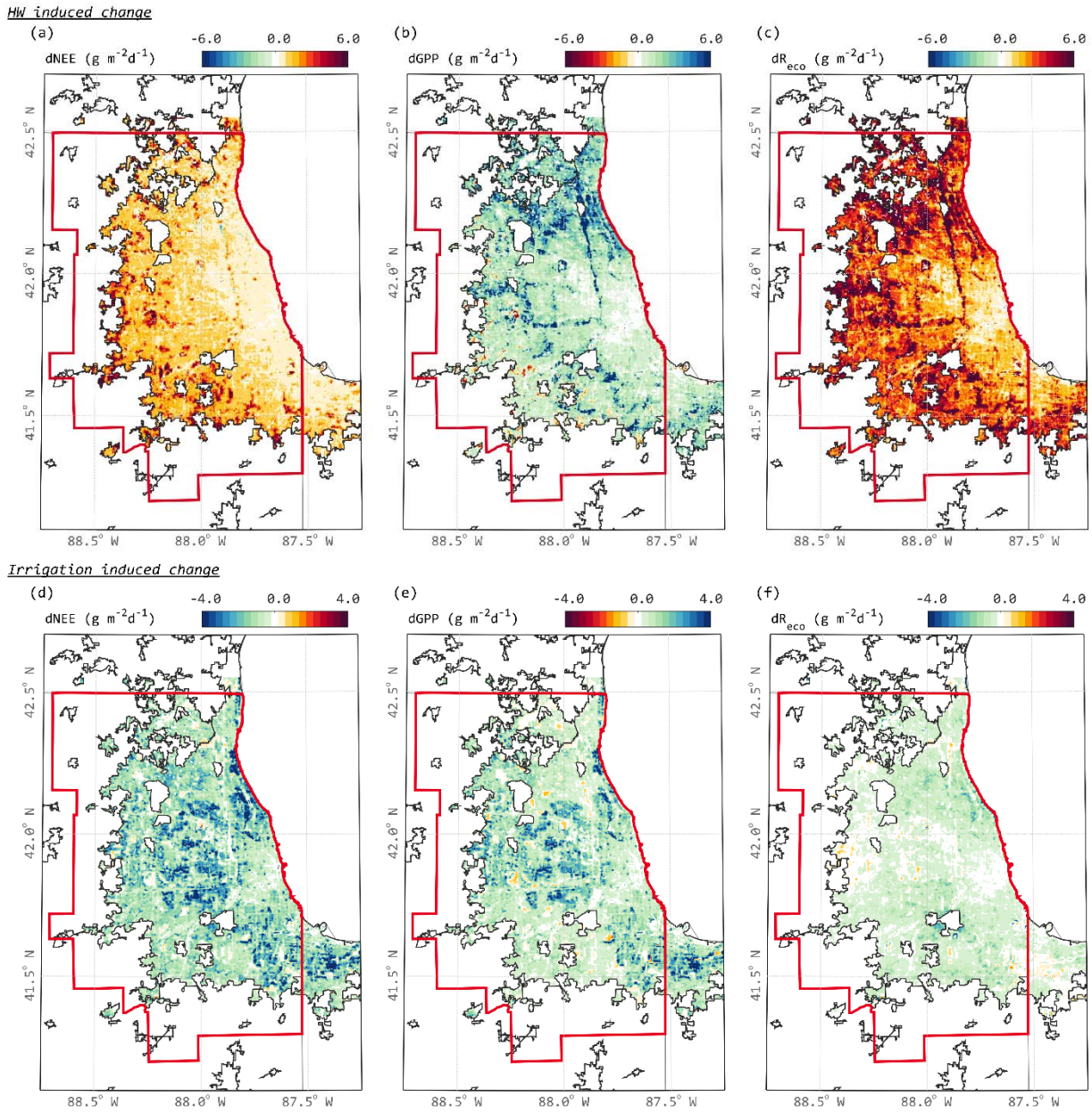
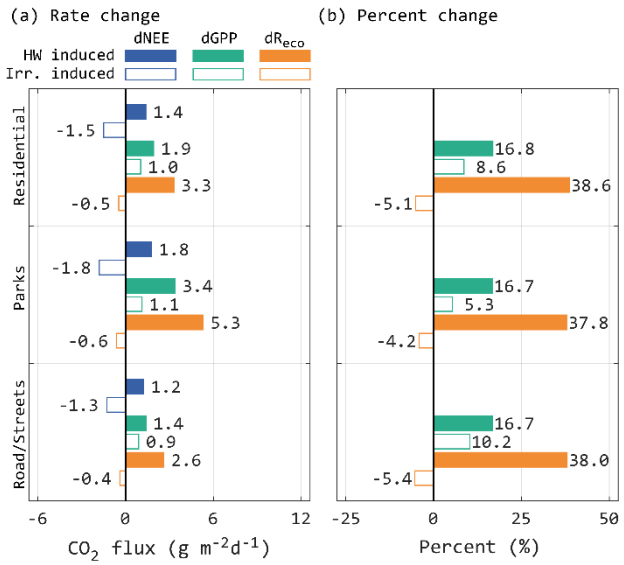



**Figure 6. Maps of the impacts on $CO_2$ exchanges from environmental and anthropogenic perturbations**. **(a-c)** Impacts of heatwave on NEE, GPP, $R_{eco}$, respectively; and **(d-f)** impacts of irrigation on NEE, GPP, $R_{eco}$, respectively. The color bars are adjusted for each subplot. Cool colors (green and blue) indicate positive environmental impacts (additional $CO_2$ sequestration), while warm colors (yellow and red) indicate negative environmental impacts (additional $CO_2$ release).




602

603 **Figure 7.** Change of **biogenic $CO_2$ fluxes under environmental and anthropogenic**
604 **perturbations.** Rate **(a)** and percent **(b)** changes of dNEE, dGPP, and $dR_{eco}$ due to heatwave
605 (solid bars) and irrigation (hollow bars). Blue, green, and orange colors represent dNEE, dGPP,
606 and $dR_{eco}$, respectively. See Fig. S4 for the full chart of other categories (commercial,
607 institutional, industrial, transportation, undeveloped).

608

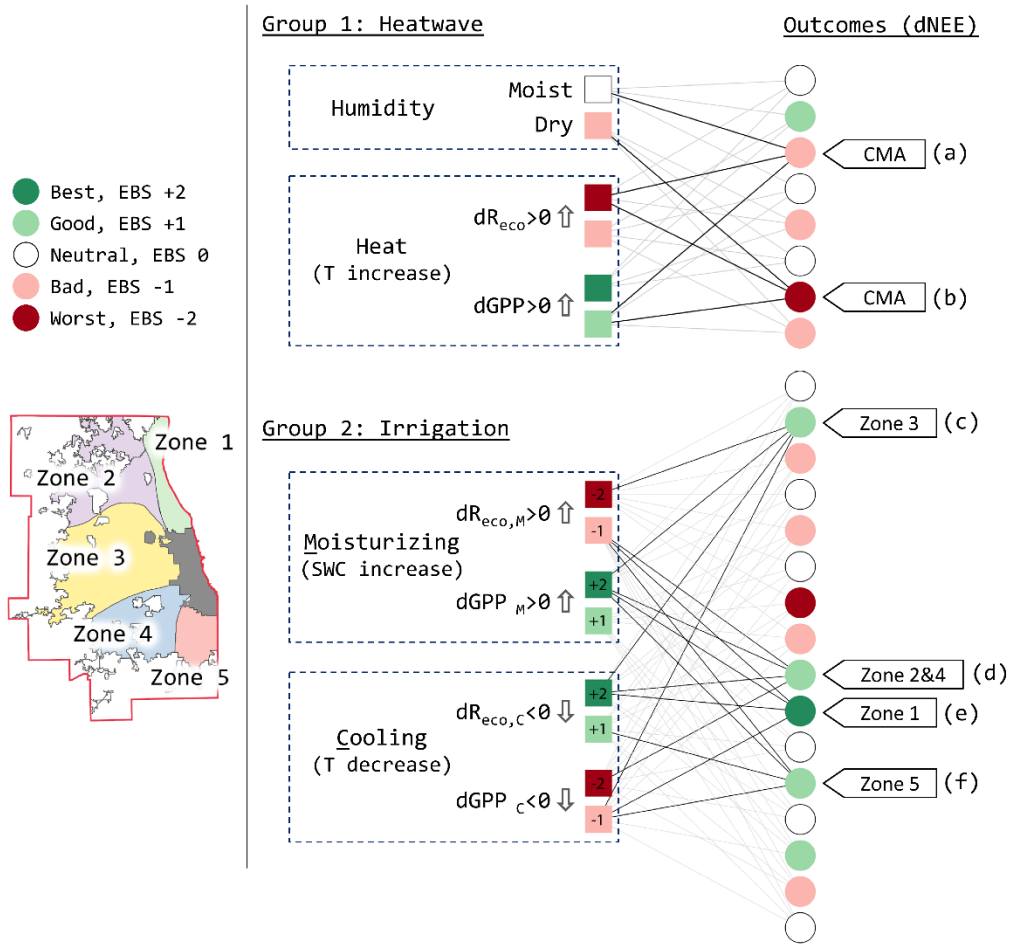



**Figure 8. Governing mechanisms on biogenic $CO_2$ exchange under environmental and anthropogenic perturbations.** The environmental impacts are summarized using Environmental Benefit Scores (EBS) for the change due to heatwaves (**Group 1**) and irrigation (**Group 2**). **(a-f)** denote the specific examples of EBS in CMA and its subzones. Both perturbations have direct impacts on water supply and temperature, leading to the changes of GPP and $R_{eco}$ (square nodes). Circle nodes represent the possible outcomes from the combinations of competing mechanisms (see section 3.4). Red colors denote additional $CO_2$ emission under environmental perturbations, while green colors denote additional $CO_2$ sequestration.

## References


Bergeron, O. and Strachan, I.B. (2011) CO2 sources and sinks in urban and suburban areas of a northern mid-latitude city. *Atmospheric Environment.* **45** 8 1564-1573. http://doi.org/10.1016/j.atmosenv.2010.12.043

Broadbent, A.M., et al. (2018) The cooling effect of irrigation on urban microclimate during heatwave conditions. *Urban Climate.* **23** 309-329. http://doi.org/10.1016/j.uclim.2017.05.002

Castán Broto, V. and Westman, L.K. (2020) Ten years after Copenhagen: Reimagining climate change governance in urban areas. *WIREs Climate Change.* **11** 4 e643. http://doi.org/10.1002/wcc.643

Chen, F., et al. (2011) The integrated WRF/urban modelling system: development, evaluation, and applications to urban environmental problems. *International Journal of Climatology.* **31** 2 273-288. http://doi.org/10.1002/joc.2158

City of Chicago (2019) Greenhouse gas inventory report - Calendar year 2017. AECOM. 34 pp.

City of Chicago (2022) 2022 Chicago Climate Action Plan. 165 pp.

Churkina, G. (2016) The Role of Urbanization in the Global Carbon Cycle. *Frontiers in Ecology and Evolution.* **3** http://doi.org/10.3389/fevo.2015.00144

Conry, P., et al. (2015) Chicago's heat island and climate change: Bridging the scales via dynamical downscaling. *Journal of Applied Meteorology and Climatology.* **54** 7 1430-1448. http://doi.org/https://doi.org/10.1175/JAMC-D-14-0241.1

Crawford, B., et al. (2011) Five years of carbon dioxide fluxes measurements in a highly vegetated suburban area. *Atmospheric Environment.* **45** 4 896-905. http://doi.org/10.1016/j.atmosenv.2010.11.017

Crum, S.M., et al. (2016) Landscape position influences soil respiration variability and sensitivity to physiological drivers in mixed-use lands of Southern California, USA. *Journal of Geophysical Research: Biogeosciences.* **121** 10 2530-2543. http://doi.org/10.1002/2016JG003469

Decina, S.M., et al. (2016) Soil respiration contributes substantially to urban carbon fluxes in the greater Boston area. *Environmental Pollution.* **212** 433-439. http://doi.org/10.1016/j.envpol.2016.01.012

649 Frantzeskaki, N., et al. (2019) Nature-based solutions for urban climate change adaptation:
650 Linking science, policy, and practice communities for evidence-based decision-making.
651 *BioScience.* **69** 6 455-466. http://doi.org/10.1093/biosci/biz042
652 Fu, P., et al. (2021) Enhanced drought resistance of vegetation growth in cities due to urban heat,
653 $CO_2$ domes and $O_3$ troughs. *Environmental Research Letters.* **16** 12 124052.
654 http://doi.org/10.1088/1748-9326/ac3b17
655 Georgescu, M., et al. (2014) Urban adaptation can roll back warming of emerging megapolitan
656 regions. *Proceedings of the National Academy of Sciences.* **111** 8 2909-2914.
657 http://doi.org/doi:10.1073/pnas.1322280111
658 Goret, M., et al. (2019) Inclusion of $CO_2$ flux modelling in an urban canopy layer model and an
659 evaluation over an old European city centre. *Atmospheric Environment: X.* **3**
660 http://doi.org/10.1016/j.aeaoa.2019.100042
661 Gourdji, S.M., et al. (2022) A Modified Vegetation Photosynthesis and Respiration Model
662 (VPRM) for the Eastern USA and Canada, Evaluated With Comparison to Atmospheric
663 Observations and Other Biospheric Models. *Journal of Geophysical Research:*
664 *Biogeosciences.* **127** 1 e2021JG006290.
665 http://doi.org/https://doi.org/10.1029/2021JG006290
666 Gurney, K.R., et al. (2020) The Vulcan version 3.0 high-resolution fossil fuel $CO_2$ emissions for
667 the United States. *Journal of Geophysical Research: Atmospheres.* **125** 19
668 e2020JD032974. http://doi.org/10.1029/2020JD032974
669 Hardiman, B.S., et al. (2017) Accounting for urban biogenic fluxes in regional carbon budgets.
670 *Science of The Total Environment.* **592** 366-372.
671 http://doi.org/https://doi.org/10.1016/j.scitotenv.2017.03.028
672 Hundertmark, W.J., et al. (2021) Influence of landscape management practices on urban
673 greenhouse gas budgets. *Carbon Balance and Management.* **16** 1 1.
674 http://doi.org/10.1186/s13021-020-00160-5
675 Jacobson, A.R., et al. (2020). CarbonTracker CT2019B, NOAA Global Monitoring Laboratory.
676 http://dx.doi.org/10.25925/z1gj-3254
677 Järvi, L., et al. (2019) Spatial Modeling of Local-Scale Biogenic and Anthropogenic Carbon
678 Dioxide Emissions in Helsinki. *Journal of Geophysical Research: Atmospheres.* **124** 15
679 8363-8384. http://doi.org/https://doi.org/10.1029/2018JD029576

680 Kabisch, N., et al. (2017). *Nature-Based Solutions to Climate Change Adaptation in Urban*
681 *Areas: Linkages between Science, Policy and Practice*, Springer Open.
682 Kindler, M., et al. (2022) Water conservation potential of modified turf grass irrigation in urban
683 parks of Phoenix, Arizona. *Ecohydrology.* **15** 3 e2399.
684 http://doi.org/https://doi.org/10.1002/eco.2399
685 Lei, N. and Han, J. (2020) Effect of precipitation on respiration of different reconstructed soils.
686 *Scientific Reports.* **10** 1 7328. http://doi.org/10.1038/s41598-020-63420-x
687 Li, P. and Wang, Z.-H. (2020) Modeling carbon dioxide exchange in a single-layer urban canopy
688 model. *Building and Environment.* **184** 107243.
689 http://doi.org/10.1016/j.buildenv.2020.107243
690 Li, P. and Wang, Z.-H. (2021) Environmental co-benefits of urban greening for mitigating heat
691 and carbon emissions. *Journal of Environmental Management.* **293** 112963.
692 http://doi.org/10.1016/j.jenvman.2021.112963
693 Li, P., et al. (2022) Multi-objective optimization of urban environmental system design using
694 machine learning. *Computers, Environment and Urban Systems.* **94** 101796.
695 http://doi.org/10.1016/j.compenvurbsys.2022.101796
696 Li, X. and Xiao, J. (2019) Mapping photosynthesis solely from solar-induced chlorophyll
697 fluorescence: A global, fine-resolution dataset of gross primary production derived from
698 OCO-2. *Remote Sensing.* **11** 21 2563. http://doi.org/10.3390/rs11212563
699 Liu, B., et al. (2021) Optimal water use strategies for mitigating high urban temperatures.
700 *Hydrology and Earth System Sciences.* **25** 1 387-400. http://doi.org/10.5194/hess-25-387-
701 2021
702 Liu, H.Z., et al. (2012) Four-year (2006–2009) eddy covariance measurements of $CO_2$ flux over
703 an urban area in Beijing. *Atmospheric Chemistry and Physics.* **12** 17 7881-7892.
704 http://doi.org/10.5194/acp-12-7881-2012
705 Livesley, S.J., et al. (2021) Water smart cities increase irrigation to provide cool refuge in a
706 climate crisis. *Earth's Future.* **9** 1 e2020EF001806. http://doi.org/10.1029/2020EF001806
707 Madani, N., et al. (2017) Improving global gross primary productivity estimates by computing
708 optimum light use efficiencies using flux tower data. *Journal of Geophysical Research:*
709 *Biogeosciences.* **122** 11 2939-2951. http://doi.org/https://doi.org/10.1002/2017JG004142

Madani, N., et al. (2020) Recent amplified global gross primary productivity due to temperature increase is offset by reduced productivity due to water constraints. *AGU Advances.* **1** 4 e2020AV000180. http://doi.org/10.1029/2020AV000180

Makra, E. and Gardiner, N. (2021) Climate Action Plan for the Chicago Region. Metropolitan Mayors Caucus, NOAA and U.S. Climate Resilience Toolkit. 110 pp.

McHale, M.R., et al. (2017) Carbon lost and carbon gained: a study of vegetation and carbon trade-offs among diverse land uses in Phoenix, Arizona. *Ecological Applications.* **27** 2 644-661. http://doi.org/10.1002/eap.1472

McPherson, E.G., et al. (2013) A new approach to quantify and map carbon stored, sequestered and emissions avoided by urban forests. *Landscape and Urban Planning.* **120** 70-84. http://doi.org/https://doi.org/10.1016/j.landurbplan.2013.08.005

Melillo, J.M., et al. (2014) Highlights of Climate Change Impacts in the United States: The Third National Climate Assessment. U.S. Global Change Research Program. 148 pp.

Menzer, O. and McFadden, J.P. (2017) Statistical partitioning of a three-year time series of direct urban net $CO_2$ flux measurements into biogenic and anthropogenic components. *Atmospheric Environment.* **170** 319-333. http://doi.org/10.1016/j.atmosenv.2017.09.049

Miller, D.L., et al. (2018) Gross primary productivity of a large metropolitan region in midsummer using high spatial resolution satellite imagery. *Urban Ecosystems.* **21** 5 831-850. http://doi.org/10.1007/s11252-018-0769-3

Ng, B.J.L., et al. (2015) Carbon fluxes from an urban tropical grassland. *Environmetnal Pollution.* **203** 227-234. http://doi.org/10.1016/j.envpol.2014.06.009

Oke, T.R., et al. (2017). *Urban Climates*. Cambridge, Cambridge University Press.

Park, C., et al. (2022) Spatiotemporal variations in urban $CO_2$ flux with land-use types in Seoul. *Carbon Balance and Management.* **17** 1 3. http://doi.org/10.1186/s13021-022-00206-w

Patel, P., et al. (2023) Deep learning based urban morphology for city-scale environmental modeling. *PNAS Nexus.* **2** 3. http://doi.org/10.1093/pnasnexus/pgad027

Perkins-Kirkpatrick, S.E. and Lewis, S.C. (2020) Increasing trends in regional heatwaves. *Nature Communications.* **11** 1 3357. http://doi.org/10.1038/s41467-020-16970-7

Reichstein, M., et al. (2005) On the separation of net ecosystem exchange into assimilation and ecosystem respiration: review and improved algorithm. *Global Change Biology.* **11** 9 1424-1439. http://doi.org/https://doi.org/10.1111/j.1365-2486.2005.001002.x

741 Ronda, R.J., et al. (2001) Representation of the canopy conductance in modeling the surface
742 energy budget for low vegetation. *Journal of Applied Meteorology.* **40** 8 1431-1444.
743 http://doi.org/10.1175/1520-0450(2001)040<1431:ROTCCI>2.0.CO;2
744 Rossini, M., et al. (2012) Remote sensing-based estimation of gross primary production in a
745 subalpine grassland. *Biogeosciences.* **9** 7 2565-2584. http://doi.org/10.5194/bg-9-2565-
746 2012
747 Salgueiro, V., et al. (2020) Annual and seasonal variability of greenhouse gases fluxes over
748 coastal urban and suburban areas in Portugal: Measurements and source partitioning.
749 *Atmospheric Environment.* **223** http://doi.org/10.1016/j.atmosenv.2019.117204
750 Seto, K.C., et al. (2012) Global forecasts of urban expansion to 2030 and direct impacts on
751 biodiversity and carbon pools. *Proceedings of the National Academy of Sciences U.S.A.*
752 **109** 40 16083-16088. http://doi.org/10.1073/pnas.1211658109
753 Sharma, A., et al. (2016) Green and cool roofs to mitigate urban heat island effects in the
754 Chicago metropolitan area: evaluation with a regional climate model. *Environmental*
755 *Research Letters.* **11** 6 064004. http://doi.org/10.1088/1748-9326/11/6/064004
756 Sharma, A., et al. (2017) Urban meteorological modeling using WRF: a sensitivity study.
757 *International Journal of Climatology.* **37** 4 1885-1900.
758 http://doi.org/https://doi.org/10.1002/joc.4819
759 Sharma, A., et al. (2021) The need for urban-resolving climate modeling across scales. *AGU*
760 *Advances* **2** 1 http://doi.org/10.1029/2020av000271
761 Skamarock, W.C., et al. (2019). A description of the advanced research WRF model version 4.
762 http://doi.org/10.6084/m9.figshare.7369994.v4
763 Smith, I.A., et al. (2019) Live fast, die young: Accelerated growth, mortality, and turnover in
764 street trees. *PLoS One.* **14** 5 e0215846. http://doi.org/10.1371/journal.pone.0215846
765 Stagakis, S., et al. (2019) Eddy covariance measurements and source partitioning of $CO_2$
766 emissions in an urban environment: Application for Heraklion, Greece. *Atmospheric*
767 *Environment.* **201** 278-292. http://doi.org/10.1016/j.atmosenv.2019.01.009
768 Tomimatsu, H. and Tang, Y. (2016) Effects of high $CO_2$ levels on dynamic photosynthesis:
769 carbon gain, mechanisms, and environmental interactions. *Journal of Plant Research.*
770 **129** 3 365-377. http://doi.org/10.1007/s10265-016-0817-0

UN-Habitat (2020) World City Report 2020: The Value of Sustainable Urbanization. United Nations Human Sattlement Programme. 377 pp.

Vahmani, P. and Ban-Weiss, G.A. (2016) Impact of remotely sensed albedo and vegetation fraction on simulation of urban climate in WRF-urban canopy model: A case study of the urban heat island in Los Angeles. *Journal of Geophysical Research: Atmospheres.* **121** 4 1511-1531. http://doi.org/https://doi.org/10.1002/2015JD023718

Vavrus, S. and Van Dorn, J. (2010) Projected future temperature and precipitation extremes in Chicago. *Journal of Great Lakes Research.* **36** 22-32. http://doi.org/https://doi.org/10.1016/j.jglr.2009.09.005

Velasco, E. and Roth, M. (2010) Cities as Net Sources of CO2: Review of atmospheric $CO_2$ exchange in urban environments measured by eddy covariance technique. *Geography Compass.* **4** 9 1238-1259. http://doi.org/https://doi.org/10.1111/j.1749-8198.2010.00384.x

Velasco, E., et al. (2013) The role of vegetation in the $CO_2$ flux from a tropical urban neighbourhood. *Atmospheric Chemistry and Physics.* **13** 20 10185-10202. http://doi.org/10.5194/acp-13-10185-2013

Wang, C., et al. (2021) A single-layer urban canopy model with transmissive radiation exchange between trees and street canyons. *Building and Environment* **191** http://doi.org/10.1016/j.buildenv.2021.107593

Wang, C., et al. (2018) Cooling effect of urban trees on the built environment of Contiguous United States. *Earth's Future.* **6** 8 1066-1081. http://doi.org/https://doi.org/10.1029/2018EF000891

Wang, C., et al. (2019a) Urban water capacity: Irrigation for heat mitigation. *Computers, Environment and Urban Systems.* **78** 101397. http://doi.org/10.1016/j.compenvurbsys.2019.101397

Wang, S., et al. (2019b) Urban−rural gradients reveal joint control of elevated $CO_2$ and temperature on extended photosynthetic seasons. *Nature Ecology & Evolution.* **3** 7 1076-1085. http://doi.org/10.1038/s41559-019-0931-1

Wu, D., et al. (2021) A model for urban biogenic $CO_2$ fluxes: Solar-induced fluorescence for modeling urban biogenic fluxes (SMUrF v1). *Geoscientific Model Development.* **14** 6 3633-3661. http://doi.org/10.5194/gmd-14-3633-2021

802 Wuebbles, D., et al. (2021) An assessment of the impacts of climate change in Illinois. The
803 Nature Conservancy in Illinois. 191 pp. https://doi.org/10.13012/B2IDB-1260194_V1
804 Wuebbles, D., et al. (2019) An assessment of the impacts of climate change on the Great Lakes.
805 Environmental Law & Policy Center. 70 pp.
806 Xu, H., et al. (2020) Heatwave effects on gross primary production of northern mid-latitude
807 ecosystems. *Environmental Research Letters.* **15** 7 074027. http://doi.org/10.1088/1748-
808 9326/ab8760
809 Yang, J. and Wang, Z.-H. (2015) Optimizing urban irrigation schemes for the trade-off between
810 energy and water consumption. *Energy and Buildings.* **107** 335-344.
811 http://doi.org/10.1016/j.enbuild.2015.08.045
812 Yi, C., et al. (2010) Climate control of terrestrial carbon exchange across biomes and continents.
813 *Environmental Research Letters.* **5** 3 034007. http://doi.org/10.1088/1748-
814 9326/5/3/034007
815 Zhao, M. and Running, S.W. (2010) Drought-induced reduction in global terrestrial net primary
816 production from 2000 through 2009. *Science.* **329** 5994 940-943.
817 http://doi.org/doi:10.1126/science.1192666
818 Zhao, S., et al. (2016) Prevalent vegetation growth enhancement in urban environment.
819 *Proceedings of the National Academy of Sciences U.S.A.* **113** 22 6313-6318.
820 http://doi.org/10.1073/pnas.1602312113
821 Zhou, D., et al. (2016) Remotely sensed assessment of urbanization effects on vegetation
822 phenology in China's 32 major cities. *Remote Sensing of Environment.* **176** 272-281.
823 http://doi.org/10.1016/j.rse.2016.02.010

824

825